Short-term magma-carbonate interaction: A modelling perspective

Simone Colucci [a],*, Federico Brogi [a], Gianluca Sottili [b], Chiara P. Montagna [a], Paolo Papale [a]

[a] *Istituto Nazionale di Geofisica e Vulcanologia, via Cesare Battisti, 53, Pisa, 56125, Italy*
[b] *Dipartimento di Scienze della Terra, Sapienza Università di Roma, Piazzale Aldo Moro, 5, Roma, 00185, Italy*

ARTICLE INFO

ABSTRACT

Short-term interaction of magma with crustal carbonates can affect a volcano's eruptive style and drive even low-viscosity magmas toward large explosive eruptions. Only a few studies have focused on short-term magma-carbonate interaction under controlled laboratory conditions and the physical processes behind the experimental observations are still poorly understood. In this work, we present the first numerical modelling study of short-term magma-carbonate interaction and provide an interpretative framework for experimental and field observations. We developed thermodynamic and dynamic models for carbonate dissolution and mixing and mingling between contaminated magma pockets and host magma. We find that mixing and mingling can play a central role in modulating the efficiency of volatile exsolution. The increasing viscosity of the host melt slows down melt mingling and hence the mixing process, limiting volatile exsolution. Less efficient mixing and mingling could allow the fingerprints of short-term magma-carbonate interaction to be preserved in volcanic and intrusive rocks. Finally, we highlight that the mechanism and timescale of magma-carbonate interaction open a key question about the anomalous high mobility of CaO during carbonate dissolution.

1. Introduction

Interaction between magma and crustal carbonates can alter magma's physical properties (e.g., density, viscosity) and increase its volatile budget, with potentially relevant impacts on volcanic unrest and eruptive dynamics. Volcanoes sitting on carbonate basements that show evidence of such interactions include but are not limited to Colli Albani, Italy (Sottili et al., 2010; Freda et al., 2011; Di Rocco et al., 2012; Gozzi et al., 2014), Somma-Vesuvius, Italy (Iacono-Marziano et al., 2009; Jolis et al., 2013), Merapi, Indonesia (Troll et al., 2012; Whitley et al., 2020; Deegan et al., 2023), Popocatepetl, Mexico (Goff et al., 2001). During magma transport and emplacement in the crust, carbonate xenoliths can be entrained and assimilated (Deegan et al., 2010; Sottili et al., 2010; Jolis et al., 2013; Carter and Dasgupta, 2016; Knuever et al., 2022; Deegan et al., 2022). Around magmatic intrusions emplaced into carbonate-bearing rocks, contact metamorphism can lead to metasomatism, skarn formation, and decarbonation of the host rocks (e.g., Gaeta et al., 2009; Mollo et al., 2010; Di Rocco et al., 2012; Lustrino et al., 2022). These interactions may occur on different timescales, ranging from thousands of years to seconds.

Short-term magma-carbonate interaction has been proposed as a plausible mechanism to trigger eruptions and enhance the explosivity of low-silica magmas (Deegan et al., 2010; Freda et al., 2011; Troll et al., 2012; Jolis et al., 2013; Blythe et al., 2015; Knuever et al., 2022). For instance, at Merapi volcano, during the 2006 eruption, there is geochemical evidence of fluctuating peaks of carbon dioxide, released by a carbonate source, that coincides with increasing eruptive intensity (Troll et al., 2012). Furthermore, petrographic and geochemical data, supported by experiments and thermal modelling, on the Pozzolane Rosse eruption, the largest mafic explosive event at the Colli Albani volcanic district (Italy), provide evidence for significant ingestion of carbonate wall rocks during magma ascent, that may have had an impact on the eruption explosivity (Sottili et al., 2010; Freda et al., 2011).

Experimental studies show that dissolution of carbonate clasts in magma generates Ca-enriched contaminated melts separated from the host melt by a mixing front (Deegan et al., 2010; Jolis et al., 2013; Blythe et al., 2015; Hamann et al., 2018). The properties of the contaminated melt are strongly different from the original melt, due to calcium enrichment: the depolymerisation effect of CaO has been found to decrease melt viscosity below 1 Pa s (Deegan et al., 2010); moreover, the high affinity of calcium with carbon dioxide substantially increases the capability of the contaminated melt to dissolve CO_2 (Papale et al., 2022). Also, the non-solubilized CO_2, produced by carbonate dissolution, generates gas bubbles that nucleate at the interface with the

---

* Corresponding author.
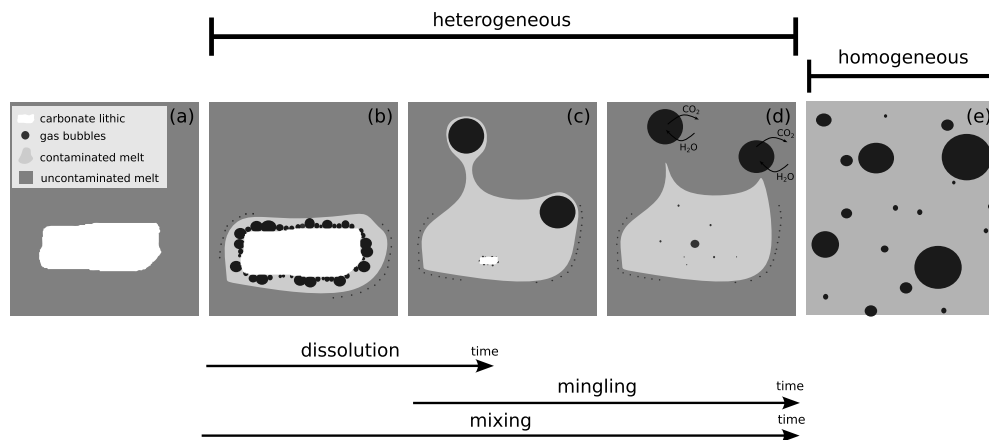*E-mail address:* simone.colucci@ingv.it (S. Colucci).

Fig. 1. Conceptual drawing of short-term magma-carbonate interaction. a) The magma can pick up fragments of carbonate rocks as it rises to the surface; b) the melt shell around the clast is contaminated in CaO and CO_2 and CO_2-rich gas bubbles nucleate and grow at the melt-clast interface; c) the bubble rising stretches the contaminated melt promoting mingling between contaminated and host melt; d) once migrated outside of the contaminated region, the CO_2-rich gas bubbles interact with the host magma; additional gas bubbles are observed at the interface between the two melts; e) When the mixing is complete new gas and melts phases are expected.

carbonate clast. Bubbles grow by diffusion and coalescence and migrate away from the contaminated melt region when buoyancy becomes large enough to allow for mechanical separation from the melt phase. Bubble migration is a viable mechanism to promote mechanical mingling between the contaminated melt and the host magma (Deegan et al., 2010; Blythe et al., 2015). The bubble-rising process stretches the contaminated melt, generating filaments that can diffuse in a short timescale, hence strongly catalysing magma mixing (Wiesmaier et al., 2015).

All the aforementioned works provide important observations on the kinetics of carbonate dissolution in silicate melts as well as on melt mingling and mixing dynamics. However, the derived dissolution timescales are limited to a narrow range of experimental conditions, and a quantitative estimation of the released gas amount is still missing. Also, the role of mixing and mingling in controlling gas exsolution is not quantified and the related timescales are not constrained.

The aim of this work is to model numerically carbonate clast dissolution, mechanical mingling and chemical mixing and infer their timescales. We also performed thermodynamic calculations to constrain the exsolved amount of volatiles, both at the outset of the interaction and after the homogenisation process is complete.

2. Review of current conceptual model

Fragments of carbonate rocks can be picked up by magma during emplacement and transport to the surface (Fig. 1a). A critical aspect regards the pressure dependence of the decomposition temperature of $CaCO_3$. Thermal decomposition of $CaCO_3$ in solid CaO and gaseous CO_2 occurs above ~ 1120 K at atmospheric pressure conditions (Knuever et al., 2022, 2023). When pressure exceeds a few MPa, thermal decomposition occurs at much higher temperatures (Baker, 1962; Peretyazhko et al., 2021). In particular, at pressure (p) and temperature (T) conditions representative of a magmatic plumbing system ($p < 1$ GPa, 1000 K $< T <$ 1400 K) carbonate exists as an amorphous solid phase (Baker, 1962; Hou et al., 2019; Peretyazhko et al., 2021). As a consequence, thermal decomposition is limited to a very shallow depth while metamorphic decarbonation and dissolution process (i.e., interface reaction + diffusion), leading to carbonate assimilation, are important from the deeper parts of the plumbing system to the conduit. Although magma-carbonate interaction experiments are performed only at 500 MPa (e.g., Deegan et al., 2010; Jolis et al., 2013), 150 MPa experiments on magma-carbonaceous shale interaction (Deegan et al., 2022) confirm that dissolution predominates over thermal decomposition. During carbonate xenolith assimilation, the melt shell around the clast becomes contaminated in both CaO and CO_2 via diffusion (Fig. 1b) and CO_2

gas bubbles nucleate and grow at the melt-clast interface (Fig. 1b). Initially, the bubbles are embedded in the contaminated region. Then, when they are large enough for the buoyancy force to overcome viscous forces, they rise, stretching the contaminated melt and generating thin filaments (Fig. 1c), promoting mingling between the contaminated and the host melt (Deegan et al., 2010; Blythe et al., 2015; Wiesmaier et al., 2015). These thin filaments can diffuse out in the melt on a relatively short timescale. The CO_2-rich gas bubbles, when migrated outside of the contaminated region, will interact with the uncontaminated host melt exchanging volatiles (Fig. 1d). Additional gas bubbles are also observed in the previously published magma-carbonate interaction experiments at the interface between the contaminated and uncontaminated melts (Fig. 1b-d). These bubbles are interpreted as due to bubble migration from the contaminated Ca-rich melt, or to heterogeneous bubble nucleation on microlite surfaces (Deegan et al., 2010; Jolis et al., 2013; Blythe et al., 2015). When mixing between the contaminated and the host melt is complete, new gas and melt phases are present (Fig. 1e).

The timescales of clast dissolution, mingling and mixing are represented by the arrows at the bottom of Fig. 1. Even if the timescales are not well constrained, experiments (Deegan et al., 2010; Jolis et al., 2013; Blythe et al., 2015) suggest the following relation

$$\tau_{dis} \leq \tau_{min} < \tau_{mix}. \tag{1}$$

The timescale of carbonate dissolution (τ_{dis}) observed in the experiments is in the order of seconds to minutes, for clasts with a millimetric length scale, and it increases with increasing viscosity of the uncontaminated melt (Deegan et al., 2010; Jolis et al., 2013; Blythe et al., 2015). The timescale of the mingling process (τ_{min}) depends on the viscosity of the host magma and the bubble size. The mixing timescale (τ_{mix}) depends on the mass diffusivity of the melt oxides, as well as on the square of the diffusive length scale, which is the characteristic length of a contaminated melt filament. Therefore, mechanical mingling controls the timescales of mixing by thinning the contaminated melt pocket (Wiesmaier et al., 2015). In summary, all these three time scales are intimately related to melt diffusion and viscosity. Decreasing diffusion hinders dissolution and mixing dynamics; increasing viscosity hinders the dynamics of mingling. Diffusion and viscosity are inversely related by Eyring equation (e.g., González-García et al., 2017): diffusion slows down and viscosity increases as temperature and dissolved water content decrease. The dependence of the diffusion coefficient on temperature is well characterized by an exponential Arrhenius relation; the dependence on pressure is more complicated to be parameterized but

is weaker (Zhang and Gan, 2022). There is no a theoretical formulation for the dependence on melt composition and only empirical relations are available but not accurate enough for practical applications (Zhang and Gan, 2022).

3. Methods

Short-term magma-carbonate interaction process involves different subprocesses (dissolution, mingling and mixing) that may interact with one another. In this work, we adopt a timescale separation principle: processes travelling at different timescales can be studied separately, through dedicated models. In some cases, this assumption can fail (e.g., $\tau_{dis} \simeq \tau_{min}$), however, this is a valid starting point to tackle a complex problem like ours. In the following sections, we illustrate each dedicated model with equations and physical background.

3.1. Carbonate dissolution

The dissolution process of solids in liquids involves two subprocesses: the interface reaction that generates contaminated liquid and the subsequent diffusion of the contaminated liquid toward the uncontaminated one. The diffusion process moves the contaminated liquid away from the interface, allowing the reaction to continue. If diffusion is slower compared to the reaction at the interface, diffusion becomes the rate-limiting step, and the dissolution is referred to as diffusion-controlled. Since in the experiments the clast is observed to dissolve more quickly than the rate at which the concentration profile flattens, the dissolution is controlled by diffusion. Furthermore, recent experiments (Persikov et al., 2022) show that at the interaction of carbonate-bearing melts with basalts, the diffusion of carbon dioxide is very similar to the diffusion of CaO. According to this, we can model the dissolution of a spherical static carbonate clast surrounded by a shell of melt as a diffusion-controlled process by modelling the diffusion of CaO only.

The shell radius S evolves in time according to the volume conservation

$$S(t)^3 - R(t)^3 = S_0^3 - R_0^3, \tag{2}$$

where $R(t)$ is the clast radius at time t, and S_0 and R_0 are the initial shell radius and clast radius, respectively. The equations are expressed in spherical, Lagrangian coordinates. The Lagrangian coordinate x is related to the Eulerian radial coordinate r by conservation of volume

$$x^3 = r^3 - \left(R^3 - R_0^3\right). \tag{3}$$

This coordinate system has the advantage that for $r = R$, $x = R_0$ and for $r = S$, $x = S_0$, hence the computational domain is fixed during clast dissolution. The advection-diffusion equation for CaO is given by

$$\frac{\partial y_{CaO}^{melt}}{\partial t} = \frac{1}{x^2} \frac{\partial}{\partial x} \left(\frac{\left(x^3 - R_0^3 + R^3\right)^{\frac{4}{3}}}{x^2} J \right), \tag{4}$$

$$J = -D_{CaO} \frac{\partial y_{CaO}^{melt}}{\partial x}, \tag{5}$$

where y_{CaO}^{melt} is the mass fraction of CaO in the shell of melt, D is the CaO diffusion coefficient and J is the diffusive mass flux. From the mass conservation of the clast, we obtain the evolution of the clast radius (see Appendix A.1)

$$\frac{dR^3}{dt} = \frac{3}{\varepsilon_{CaO}} \frac{\rho_{melt}}{\rho_{CaCO_3}} \int_{R_0}^{S_0} x^2 \frac{dy_{CaO}^{melt}}{dt} dx, \tag{6}$$

where ρ_{melt} is the host melt density and ε_{CaO} is the ratio of the mass of CaO to CaCO$_3$ ($\varepsilon_{CaO} = 0.56$).

3.2. Chemical mixing

Chemical mixing between the contaminated and the uncontaminated melt is described by a multicomponent diffusion model for the anhydrous melt oxides combined with effective binary diffusion-reaction models for the volatile components (H$_2$O and CO$_2$). CO$_2$ is dissolved in the melt in the form of two main different species: mobile molecular CO$_2$ (CO$_2^{mol}$) and less mobile CO$_3^{2-}$ groups linked to the silicate network. From rhyolite to basalt melts, the diffusivity of CO$_2^{mol}$ increases, but the ratio CO$_2^{mol}$/CO$_3^{2-}$ decreases, leading to a total CO$_2$ diffusivity roughly independent on the anhydrous melt composition (Watson et al., 1982; Nowak et al., 2004; Baker et al., 2005; Spickenbom et al., 2010; Zhang and Ni, 2010). An interesting result for our study is reported in Baker et al. (2005), where the diffusion of CO$_2$ is evaluated at the interface of dissolving calcite. Despite a large increase in the Ca content of the melt (and therefore in depolymerisation degree) near the interface, the CO$_2$ profile is consistent with a single diffusion value, confirming the independence of CO$_2$ diffusivity on composition. Furthermore, as far as we know, there is no evidence that the diffusion of the other melt oxides depends on CO$_2$ concentration. Therefore, we choose to treat the diffusion of CO$_2$ as an effective binary diffusion. On the other side, although H$_2$O diffusion should be treated as multicomponent (González-García et al., 2017), more experimental work is needed to quantify its behaviour, which is therefore treated as effectively binary (Zhang and Ni, 2010).

The multicomponent diffusion of the anhydrous melt oxides can be described by generalizing Fick's second law according to Onsager formalism (Onsager, 1945),

$$\frac{\partial \mathbf{y}}{\partial t} = \mathbf{D} \frac{\partial^2 \mathbf{y}}{\partial x^2}, \tag{7}$$

where $\mathbf{D}$ is the diffusion matrix and $\mathbf{y}$ is the vector whose components are the mass fractions of the oxides in the anhydrous melt. Equation (7) solves for the concentration of $(n-1)$ components, thus the n-th component must be arbitrarily designated as the solvent (Cussler, 2007). The effective binary diffusion and exsolution of volatiles can be described by a reaction-diffusion equation

$$\frac{\partial[y_{H_2O}^{melt}\rho_{melt}(1-\alpha)]}{\partial t} = D_{H_2O} \frac{\partial^2}{\partial x^2}[y_{H_2O}^{melt}\rho_{melt}(1-\alpha)] - \Gamma_{H_2O} \tag{8}$$

$$\frac{\partial[y_{CO_2}^{melt}\rho_{melt}(1-\alpha)]}{\partial t} = D_{CO_2} \frac{\partial^2}{\partial x^2}[y_{CO_2}^{melt}\rho_{melt}(1-\alpha)] - \Gamma_{CO_2} \tag{9}$$

where D is the effective binary diffusion coefficient, ρ_{melt} is the melt density, α is the gas volume fraction, and $\Gamma(\mathbf{y}, y_{H_2O}^{melt}, y_{CO_2}^{melt}, y_{H_2O}^{gas}, \alpha)$ is the reaction sink/source term related to the exsolution/dissolution process (see Appendix B.2). The mass conservation of volatile species in the gas phase is given by

$$\frac{\partial(y_{H_2O}^{gas}\rho_{gas}\alpha)}{\partial t} = \Gamma_{H_2O} \tag{10}$$

$$\frac{\partial(y_{CO_2}^{gas}\rho_{gas}\alpha)}{\partial t} = \Gamma_{CO_2} \tag{11}$$

$$y_{CO_2}^{gas} = 1 - y_{H_2O}^{gas} \tag{12}$$

where $\rho_{gas}(y_{H_2O}^{gas})$ is the gas density, given by a perfect gas equation of state. Now we have $(n + 3)$ variables ($y_1^{melt},...,y_{n-1}^{melt},y_{H_2O}^{melt}, y_{CO_2}^{melt}, y_{H_2O}^{gas}, \alpha_{gas}$) for $(n + 3)$ equations (7) - (11). Equations (7)-(12) are solved by adopting a semi-numerical approach. Assuming that the interdiffusion coefficients of matrix $\mathbf{D}$ are independent of composition, Equation (7) for an infinite diffusion couple can be solved analytically (see Appendix B.1); Equations (8)-(12) are solved numerically using Matlab® (function pdepe).

Table 1

Notations and units.

Symbol	Description	Units
R	clast radius	m
S	radius of the shell of melt	m
y_i^{melt}	$\frac{\text{(mass species in melt)}}{\text{(mass melt)}}$	-
y_i^{magma}	$\frac{\text{(mass species in magma)}}{\text{(mass magma)}}$	-
y_i^{tot}	$\frac{\text{(mass species in magma + mass species in dissolved } CaCO_3)}{\text{(mass magma + mass dissolved } CaCO_3)}$	-
y_g^{tot}	$\frac{\text{(mass gas)}}{\text{(mass magma + mass dissolved } CaCO_3)}$	-
y_c^{tot}	$\frac{\text{(mass dissolved } CaCO_3)}{\text{(mass magma + mass dissolved } CaCO_3)}$	-
β	$\frac{\text{(mass contaminated magma)}}{\text{(mass contaminated magma + mass incontaminated magma)}}$	-
$\varepsilon_{CaO} = 0.56$	$\frac{\text{(mass CaO)}}{\text{(mass } CaCO_3)}$	-
$\varepsilon_{CO_2} = 0.44$	$\frac{\text{(mass } CO_2)}{\text{(mass } CaCO_3)}$	-
t	time	s
x	spatial coordinate across the contamination front	m
D	matrix of interdiffusion coefficients	$m^2 \ s^{-1}$
J	interfacial (diffusive) mass flux	$kg \ m^{-2} \ s^{-1}$
y	vector of mass fractions of anhydrous melt oxides	-
D	binary diffusion coefficient	$m^2 \ s^{-1}$
α	gas volume fraction	-
Γ	exsolution/dissolution rate	$kg \ m^{-3} \ s^{-1}$
μ	viscosity	Pa s
ρ	density	$kg \ m^{-3}$
$cont$	contaminated	
$uncont$	uncontaminated	
ht	heterogeneous	

3.3. Mingling dynamics

The mingling dynamics between a contaminated, low-viscosity, gas-rich melt pocket and an uncontaminated melt are simulated using the open-source computational fluid dynamics software OpenFOAM, which has been already tested and benchmarked on volcanological problems (Brogi et al., 2022). The numerical simulations are performed with the multiphase solver `icoReactingMultiphaseInterFoam` which can deal with multiple incompressible non-isothermal phases and phase change. However, in these simulations, we do not consider any exchange of mass and heat between the different phases. The volume of fluid method is adopted in OpenFOAM to resolve the position and shape of the interface separating two fluids or phases (e.g., liquid–gas). As already shown by Brogi et al. (2022), we remark that the details of the numerical solver and its parameters may affect the details of the interface geometry between the contaminated and uncontaminated melts. However, convergence tests and comparison with experimental observations (Appendix C.1) have demonstrated that the fluid solver reproduces well the overall dynamics of the mingling of two liquids enhanced by a rising bubble.

3.4. Thermodynamics of melt-volatile equilibria

We use SOLWCAD (Papale et al., 2006) to calculate the multi-component gas-melt equilibrium in a magma contaminated by the dissolution of carbonate. For a given pressure and temperature, SOLWCAD requires, as input, the melt composition and the volatile content (H_2O + CO_2). The total mass fractions of the melt oxides (see Table 1 for notations and units), after the dissolution of a given mass fraction of carbonate (y_c^{tot}) in the host magma, are given by

$$y_i^{tot} = \left(1 - y_c^{tot}\right) y_i^{magma}, \quad i = SiO_2, TiO_2, \dots ; i \neq CaO \tag{13}$$

$$y_{CaO}^{tot} = \left(1 - y_c^{tot}\right) y_{CaO}^{magma} + y_c^{tot} \varepsilon_{CaO} \tag{14}$$

where y_i^{magma} is the mass fraction of the melt oxide in the original host magma and ε_{CaO} is the ratio of the mass of CaO to $CaCO_3$ ($\varepsilon_{CaO} = 0.56$). The total mass fractions of H_2O and CO_2 are given by

$$y_{H_2O}^{tot} = \left(1 - y_c^{tot}\right) y_{H_2O}^{magma} \tag{15}$$

$$y_{CO_2}^{tot} = \left(1 - y_c^{tot}\right) y_{CO_2}^{magma} + y_c^{tot} \varepsilon_{CO_2}, \tag{16}$$

where ε_{CO_2} is the ratio of mass of CO_2 to $CaCO_3$ ($\varepsilon_{CO_2} = 0.44$).

In this work we refer to a heterogeneous system to indicate a two-magma system, i.e., the uncontaminated host magma and the contaminated magma pockets (Fig. 1b-c); we refer to a homogeneous system as a single-magma system (Fig. 1e), produced by complete mixing of the uncontaminated host melt with the contaminated melt and the achievement of a new state of thermodynamic equilibrium between the melt and gas phase. In the homogeneous system (i.e., t $\geq \tau_{mix}$), these expressions (equations (13)-(16)) can be used to calculate with SOLWCAD the amount of dissolved volatiles, the gas fraction and its composition, for a given pressure, temperature, composition of the original host magma (y_i^{magma}, $y_{H_2O}^{magma}$, $y_{CO_2}^{magma}$) and mass fraction of dissolved carbonate(y_c^{tot}). In the heterogeneous system, thermodynamic equilibrium imposes, as an additional constraint, no mass exchange between the region contaminated by the carbonate and the original, uncontaminated host magma. This constraint holds as long as the interface is sharp (i.e., t $\ll \tau_{mix}$) and the gas bubbles are inside the contaminated region (i.e., t $\ll \tau_{min}$, Fig. 1b). The gas-melt equilibrium in these two subsystems can be calculated by SOLWCAD once we know the melt composition and the volatile content of each region. For the uncontaminated region, the calculation is straightforward, since we already know the composition of the original host magma (y_i^{magma}, $y_{H_2O}^{magma}$, $y_{CO_2}^{magma}$). For the contaminated region, we can use equation (13) or (14) to derive the mass fraction of dissolved carbonate in the contaminated region ($\left[y_c^{tot}\right]_{cont}$) if we know from the experiments the average composition of the contaminated melt ($\left[y_i^{tot}\right]_{cont}$ or $\left[y_{CaO}^{tot}\right]_{cont}$); once we have $\left[y_c^{tot}\right]_{cont}$, we can use equations (15) and (16) to calculate the total mass fractions of volatiles in the contaminated region. Finally, the mass fraction of gas in the overall heterogeneous system ($\left[y_g^{tot}\right]_{ht}$) can be calculated by:

$$\left[y_g^{tot}\right]_{ht} = \left[y_g^{tot}\right]_{cont} \beta + \left[y_g^{tot}\right]_{uncont} (1 - \beta). \tag{17}$$

Here, $\left[y_g^{tot}\right]_{cont}$ and $\left[y_g^{tot}\right]_{uncont}$ are, respectively, the mass fraction of gas in the contaminated and uncontaminated regions, obtained by SOLWCAD; β is the ratio between the mass of the contaminated magma and the total mass and can be calculated as follows:

$$\beta = \frac{\left[y_c^{tot}\right]_{ht}}{\left[y_c^{tot}\right]_{cont}}, \tag{18}$$

where $\left[y_c^{tot}\right]_{ht}$ is a given mass fraction of dissolved carbonate in the overall heterogeneous system.

4. Results

The exploration of the main processes occurring during short-term magma-carbonate interaction starts from the analysis of the experimental observations from Deegan et al. (2010). The melt composition used in the modelling is a basaltic-andesite from Merapi volcano (Table 3 in Deegan et al. (2010), Run-sample 386-19).

4.1. Carbonate dissolution

Since diffusion is considered the rate-limiting step in the carbonate dissolution process, the selection of an appropriate value for diffusion coefficient (D in equation (5)), and its functional form, play a major role in the modelling. To calibrate the diffusion coefficient, we compare our model results with the carbonate dissolution experiments performed by Deegan et al. (2010). The experimental data available for calibration are i) the concentration profile measured along a traverse, from the clast-melt interface to the melt, at the beginning of the experiment ("time zero" in Deegan et al. (2010)) and ii) the time it takes for the solid to completely dissolve in the melt. It is worth noting that experimental timing starts as soon as the target temperature (i.e., 1473 K)
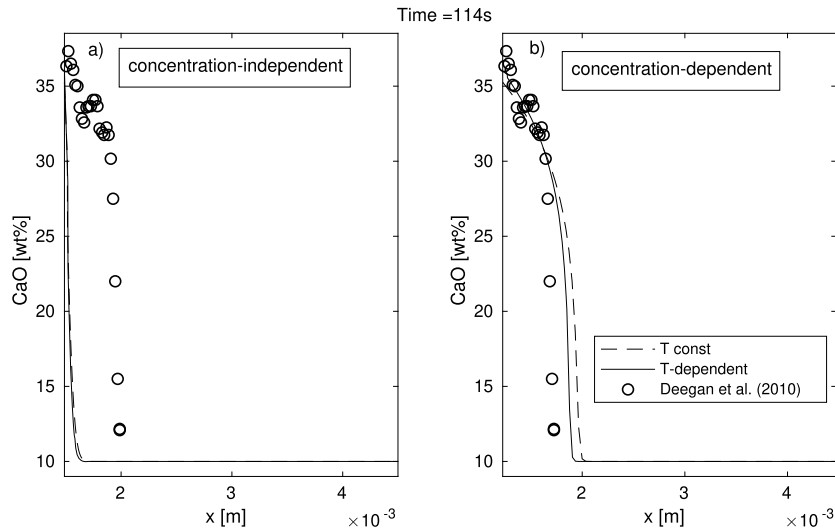
Fig. 2. Comparison between modelled (lines) and experimental (circles, Deegan et al. (2010)) concentration profiles of CaO in the melt resulting from the dissolution of $CaCO_3$ after 114 s. Solid lines: temperature changes in time, from 1273 K to 1473 K, following the experimental heating rates; dashed lines: temperature assumed constant (1473 K). On the horizontal axis the distance from the centre of the clast; the horizontal axis origin is the clast radius. a) Model results using a concentration-independent diffusion coefficient (eq. (19); D_∞ = 0.0000535 m^2 s^{-1}; E = 184096 J mol^{-1}; Hofmann and Magaritz (1977)); b) Model results using a concentration-dependent diffusion coefficient (eq. (20); K = 26; y_{CaO_0} = 0.1).

is reached. However, carbonate dissolution has already started when the target temperature is reached, during the isobaric (0.5 GPa) heating phase. During this time, which lasts 6 minutes, the dissolution dynamics will be absent (below the melting temperature, $\approx$ 1273 K) or slower than they are at 1473 K. Based on experimental heating rates (from room temperature to 1453 K: 200 degrees/min; from 1453 K to 1473 K: 20 degrees/min), we can estimate a duration of the dissolution process of 114 s, that is from the melting temperature until "time zero". During this time, the diffusion coefficient varies with temperature T following an Arrhenian relation:

$$D = D_\infty e^{-\frac{E}{RT}}, \tag{19}$$

where D_∞ is the hypothetical diffusivity at T $\to \infty$, E is the activation energy and $\tilde{R}$ is the universal gas constant. Considering the expression in equation (19) for the diffusion coefficient, the modelled concentration profile is inconsistent with the experiments (Fig. 2a, solid line) and the time required for a complete clast dissolution is five orders of magnitude higher than the experimental one. The isothermal model solution (i.e., fixing temperature at 1473 K in equation (19)) almost overlaps with the temperature-dependent one (Fig. 2a, dashed line). Hypothesizing a concentration-dependent diffusion coefficient of this form

$$D = D_0 e^{K(y_{CaO} - y_{CaO_0})}, \tag{20}$$

where D_0 is given by equation (19), K is a tuning parameter and y_{CaO_0} is the CaO concentration in the uncontaminated melt, we can perfectly reproduce the experimental concentration profile (Fig. 2b) and explain the so-called CaO pile-up (Deegan et al., 2010; Jolis et al., 2013). Again, the concentration-dependent isothermal model almost overlaps with the concentration- and temperature-dependent model: this indicates that the role of temperature is negligible compared to concentration. Furthermore, using Equation (20), a spherical clast with a 1.5 mm radius completely dissolves in a timescale consistent with the experiments.

After calibration, we can use the model to estimate the timescale of dissolution as a function of the clast radius, finding that $\tau_d \propto R^2$ (i.e., R = 1 mm: $\tau_d \sim 10^2$ s; R = 1 cm: $\tau_d \sim$ hours; R = 10 cm: $\tau_d \sim$ days). Anyway, it is worth noting that these timescales are derived from an experimental calibration at a given pressure and temperature. Even if the dependence of the diffusion on concentration seems to play a major role, compared to pressure and temperature, we believe that further

experimental investigations are necessary. Furthermore, according to literature experiments, the role of composition of the host magma seems to play an important part in the rate of dissolution.

4.2. Chemical mixing

The experiments performed by Deegan et al. (2010) show the temporal evolution of the composition measured along traverses crossing the mixing front between the contaminated melt, generated by the carbonate dissolution, and the uncontaminated host melt. We compare the results of our mixing model with their experiments after 300 s. The experiments are performed at 1473 K, 0.5 GPa, and 2 wt% of water. The high-pressure conditions employed here, dictated by the limitations of the experimental apparatus, are not expected to affect the mixing process significantly, since the diffusion coefficients are poorly dependent on pressure (Deegan et al., 2010; Guo and Zhang, 2020). The coefficients of the diffusion matrix (**D** in equation (7)) are defined according to Guo and Zhang (2020). The authors obtained a temperature-dependent diffusion matrix **D** for an 8-components (SiO_2, TiO_2, Al_2O_3, FeO, MgO, CaO, Na_2O, K_2O) basaltic melt by simultaneously fitting diffusion profiles of couple experiments at different temperatures (1533, 1773 K) and pressures (0.5-1 Gpa), by considering SiO_2 as the solvent component. In our modelling, the effective binary diffusion coefficients of volatile species (D_{H_2O} and D_{CO2} in equations (8)-(9)) are defined according to Zhang et al. (2007) and Freda et al. (2003) (Appendix B.4). The experiments of Deegan et al. (2010) that we want to reproduce are within the range of validity of these two models, except for the pressure used for evaluating D_{H_2O} (1 GPa). Nevertheless, the model of Freda et al. (2003) represents the best choice for basalt melts (Georgeais et al., 2021). Finally, it is worth noting that we are not using any tunable parameter to fit the model to the experimental data.

Given the uncertainties associated with experimental initial conditions and the range of validity of the diffusion coefficients, we can say that, overall, there is qualitative agreement between experimental and modelled concentration profiles. Experimental profiles for MgO, Na_2O and K_2O are smoother with respect to the model predictions, that show more pronounced uphill diffusion (Fig. 3e-g-h). We cannot exclude that this is a consequence of the experimental procedure used to measure the chemical profiles being 2D representations. On the other side, the behaviour of CaO, which is the most representative oxide, ranging from
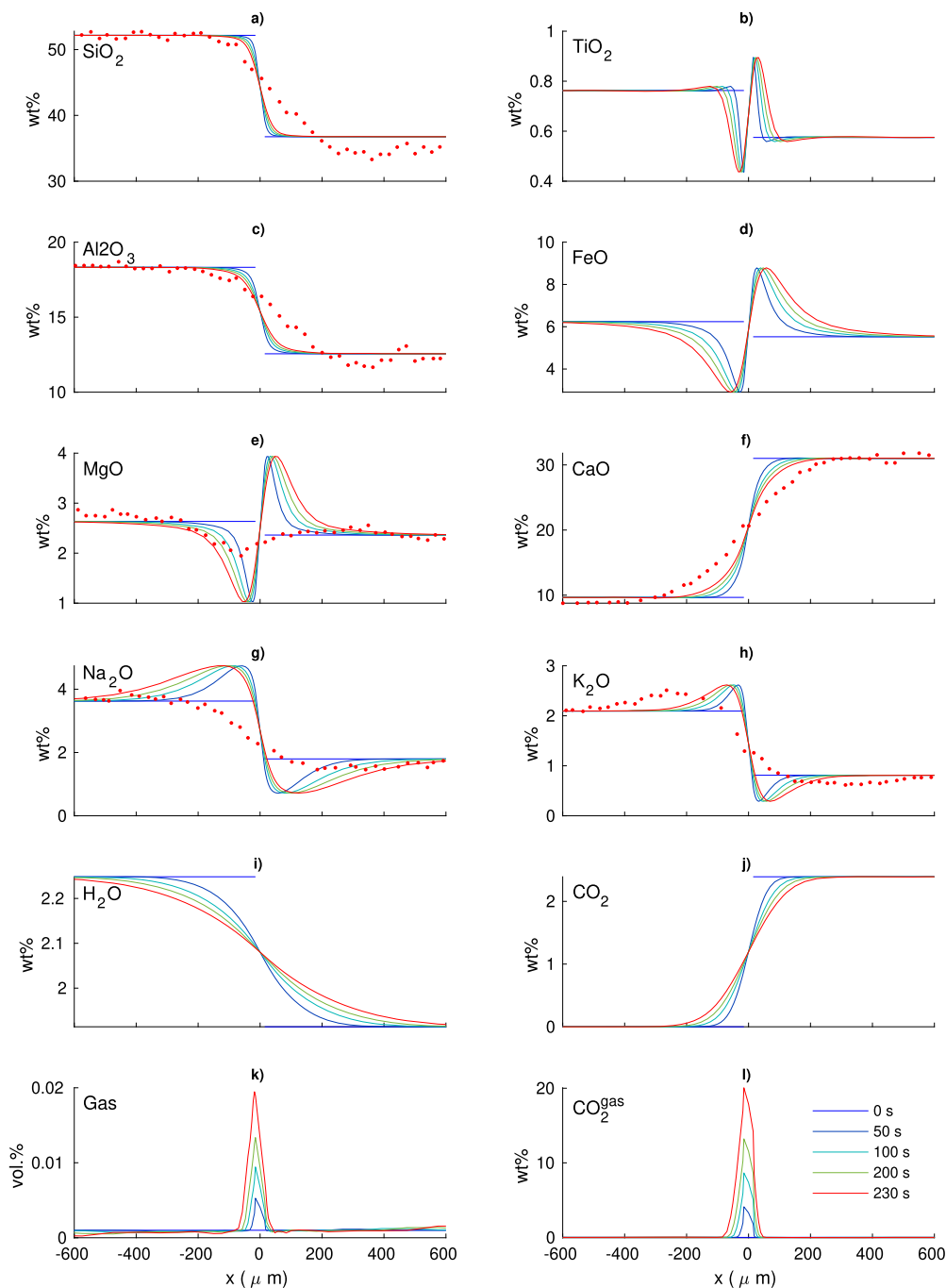
Fig. 3. Temporal evolution of the concentration profiles of the melt oxides (a-j), gas volume fraction (k), and gas composition (l), across the contamination front. Lines: model results; Points: experiments from Deegan et al. (2010) at 300 s (≈230 s after carbonate dissolution) (P = 0.5 GPa, T = 1473 K, 2 wt% of initial dissolved water).

~ 10 to ~ 30 wt%, is well reproduced by the model, as well as SiO₂ and Al₂O₃, although the latter are more scattered. In general, we can say that the length scale of the modelled diffusion profiles is consistent with the experimental data.

More importantly, our modelling takes into account the exsolution of H_2O and CO_2 as a consequence of the diffusion of the melt oxides (Fig. 3i-j-k-l). This process generates a gas wave that expands from the mixing front (Fig. 3k). This result can easily explain the experimental (Deegan et al., 2010; Jolis et al., 2013; Blythe et al., 2015) and natural (Deegan et al., 2010, 2023) observations of small bubbles at the mixing front. While the bubbles formed during the carbonate dissolution process are CO_2-rich, as will be further discussed later, the gas gener-

ated at the mixing front is H_2O-rich and progressively enriched in CO_2 (Fig. 3l). This is due to the diffusion of CO_2 from the contaminated melt (right side in Fig. 3j) to the uncontaminated melt (left side in Fig. 3j) that decreases the solubility of water determining a larger interfacial diffusive flux (Equation (B.9)) of H_2O than CO_2 toward the bubble.

The time, τ_{mix} at which molecular diffusion becomes important (mixing timescale) can be estimated as the ratio between the thickness of the contaminated melt pocket L and the diffusion coefficient D: $\tau_{mix} \sim L^2/D$. We can use a representative diffusion coefficient intermediate between the interdiffusion coefficients of CaO and SiO₂ ($D = 10^{-12}$ m² s⁻¹, Table 4 in Guo and Zhang (2020)). CaO and SiO₂ are the most representative oxides, because they are the most abundant

Table 2
Mingling simulations.

Properties	
$[\rho_{melt}]_{cont}$	2800 kg m^{-3}
$[\rho_{melt}]_{uncont}$	2600 kg m^{-3}
ρ_{gas}	500 kg m^{-3}
$[\mu_{melt}]_{cont}$	1 Pa s
$[\mu_{melt}]_{uncont}$	1-100 Pa s
μ_{gas}	4 $\cdot 10^{-5}$ Pa s
$[\alpha]_{cont}$	0.6
Initial conditions	
shell radius	9 $\cdot 10^{-3}$ m
bubble radius	7.6 $\cdot 10^{-3}$ m

in both melts, they undergo most changes from the Ca-rich to the un-contaminated melt and they are the most important in determining the solubility of H_2O and CO_2, hence volatile exsolution. If any mingling occurs, the characteristic length scale of diffusion L varies in time, as the contaminated melt pocket is thinned in one direction and stretched in the other (Fig. 1c). Therefore, the mixing time scale τ_{mix} also depends on the velocity gradient caused by the interaction dynamics between the two magmas; the latter can be estimated by simulating the bubble-enhanced mingling process.

4.3. Mingling dynamics

Magma-carbonate experiments (Deegan et al., 2010; Jolis et al., 2013; Blythe et al., 2015) show that bubbles forming in the contaminated melt, at the interface with the carbonate clast, rapidly coalesce and start to migrate, which triggers mingling between the two melts (Fig. 1c-d). The timescale of bubble-enhanced mingling can be equal to or larger than the timescale of carbonate dissolution (Equation (1)). When the dissolution timescale is large, the newly formed bubbles migrate as single bubbles moving away from one another while the clast is still dissolving; when clast dissolution is fast, the bubbles, growing close to one another, can rapidly coalesce forming larger bubbles or, in a limiting case, a single bubble. Our simulations explore the last scenario that, albeit more idealized, is not dependent on the details of the initial geometrical configuration (e.g. number and initial positions of the bubbles). Furthermore, in our modelling we do not consider the presence of a dissolving solid carbonate clast since it would require further simulation efforts. We hence assume that the dissolution is much faster than the mingling process, such that the clast is already completely dissolved at the beginning of the simulation.

The simulation setup consists of a single bubble surrounded by a shell of contaminated melt. The physical parameters and initial conditions (Table 2) are consistent with a contaminated magma pocket generated by the dissolution of 1 cm^3 carbonate clast at 200 MPa and 1273 K (corresponding, for example, to the depth of the carbonate substrate at Vesuvius, Cella et al. (2007)). We performed two different simulations by varying the viscosity of the uncontaminated host melt from 1 Pa s (consistent with the Vesuvius wet experiments of Blythe et al. (2015)) to 100 Pa s (Figs. 4, 5). The higher viscosity value can represent host melts containing 50-60 wt% of crystals (Caricchi et al., 2007) or at a lower temperature (Giordano et al., 2008).

Simulation results (Figs. 4, 5) clearly show that the bubble rises forming in its wake a filament of Ca-rich, heavier melt that gradually tapers down. The filament is stretched on one side by the rising bubble (and velocity gradients in its proximity), and on the other side by the gravity force that pulls it down. As the stretching process continues, the filament is also broken into many small droplets - we believe this is a numerical fragmentation due to the limited resolution of the mesh used for the simulations. At first, the viscosity of the host melt plays a major role in determining the timescale of this process, mainly due to different bubble rise velocities. In a few seconds for the low-

viscosity case, and hundreds of seconds for the higher-viscosity case, the filament is stretched to roughly the same length. At larger viscosities of the uncontaminated melt, the filament tends to fall under gravity forming a thick drop of heavier contaminated melt. The main difference between the two setups is the amount of contaminated melt collected in the stretching filament. In fact, the filament will be subjected to chemical diffusion on a shorter timescale, while the contaminated melt drop will require much longer time to diffuse out. For example, for a representative diffusion coefficient of $D = 10^{-12}$ m^2 s^{-1} (Section 4.2), a 1 μm thick filament will dissolve in 1 s and a 100 μm thick filament in almost 3 hours ($\tau_{mix} \sim L^2/D$). These timescales imply that, even on syn-eruptive timescales, the homogenisation process can be incomplete and contaminated melt pockets and filaments can be preserved in the volcanic deposits.

4.4. Thermodynamics of melt-volatile equilibria

The heterogeneous system for which we calculate thermodynamic phase equilibria may represent the initial state before mingling and mixing have occurred (i.e., t < τ_{mix}, τ_{min} Fig. 1b). The homogeneous system instead represents the final state, when mixing is complete (i.e., t ≥ τ_{mix}, Fig. 1e). Therefore, a comparison between the initial and final state of the system may help to quantify the importance of the mingling and mixing processes leading to homogenisation.

The chemical interaction of magma with carbonate has important effects on the melt-volatile equilibria. The dissolution of carbonate releases CaO and CO_2: the increase in CaO increases the solubility of CO_2, favouring its dissolution in the melt; the rise in CO_2 reduces the solubility of H_2O, favouring its exsolution. The interplay between CaO and CO_2 determines a slightly non-linear increase in the mass fraction of gas when increasing the proportion of interacting $CaCO_3$ (Fig. 6a), for the homogeneous (solid lines) and heterogeneous (dashed lines) systems, in both water-saturated (red colour) and water-undersaturated (blue colour) host magmas.

The water content of the host magma has a different impact on the amount of gas of homogeneous and heterogeneous systems (Fig. 6b). In homogeneous systems (solid line in Fig. 6b), the ratio between the gas mass generated by carbonate dissolution in a water-saturated host magma and the gas mass generated in an anhydrous host magma (i.e., the ratio between red and blue lines of Fig. 6a) rapidly decays by increasing the amount of interacting $CaCO_3$. That means that the initial water content of the host magma becomes more important with decreasing proportion of $CaCO_3$. This behaviour is due to water saturation that limits water vapour exsolution. In fact, the addition of CO_2 to the system, by carbonate dissolution, produces gaseous CO_2 and promotes the exsolution of water, by indirectly decreasing the water fugacity in the gas phase. At low $CaCO_3$, the gaseous CO_2 is lower or comparable with the water vapour extracted during the homogenisation; at increasing $CaCO_3$, most of the gas is CO_2, and the water contribution becomes negligible. On the other hand, in heterogeneous systems (dashed line in Fig. 6b), the role of the water content of the host magma in determining the amount of gas is always negligible. This is due to the Ca-rich composition of the contaminated melt that buffers the gas exsolution.

The gas generated by magma-carbonate interaction includes the amount produced during the dissolution, in form of gas bubbles generated at the clast-melt interface, and the one produced later, during the homogenisation by chemical mixing. The gas generated during the dissolution characterizes the heterogeneous system; the gas of the homogeneous system represents the results of the new thermodynamic equilibrium reached when mixing is complete. The ratio between the gas mass in the homogeneous system and the gas mass in the heterogeneous system can either increase or decrease, at increasing $CaCO_3$, depending on the water content of the host magma (Fig. 6c). In saturated conditions this ratio rapidly drops (Fig. 6c, red line), indicating that at low $CaCO_3$ the gaseous water extracted during the homogenisa-
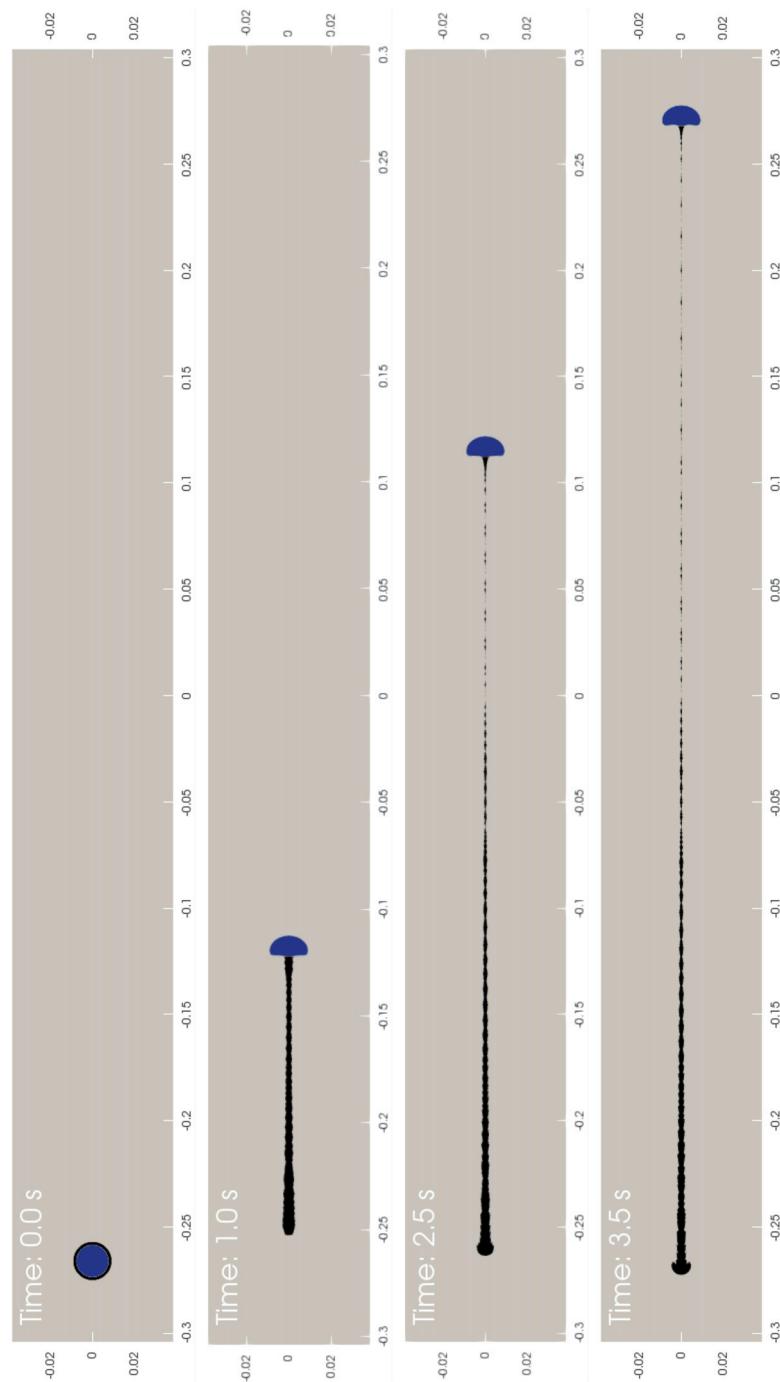
Fig. 4. Mingling simulations at 1 Pa s. In blue the CO_2 gas bubble; in black the shell of contaminated, Ca-rich melt; in grey the uncontaminated host melt. Simulation parameters are reported in Table 2.

tion is more significant or comparable with the amount of gas produced by the carbonate dissolution, already present in the heterogeneous system. On the other hand, moving towards undersaturated conditions (Fig. 6c, blue line), this ratio can assume an opposite behaviour, up to increase with the increase of $CaCO_3$. This opposite trend (decay in water-rich vs increase in water-poor) depends on the mass balance, during the homogenisation, between the CO_2 gas that dissolves back into the host magma, and the CO_2 dissolved in the contaminated magma that exsolves and favours water exsolution. During the homogenisation, the gas phase has to yield CO_2 to the melt and/or take H_2O from the melt itself. In saturated systems, H_2O exsolution prevails on CO_2 dissolution, while it is the opposite in undersaturated systems.

A similar behaviour emerges also in the composition of the gas phase (Fig. 6d): increasing the $CaCO_3$, the gas composition of the homogeneous magma (solid lines) is enriched in CO_2 because the CO_2 gas amount produced by the carbonate dissolution predominates over the gas water extracted during homogenisation. On the other hand, the heterogeneous system (dashed lines) is always richer in CO_2 because of the buffering effect of the Ca-rich composition of the contaminated melt on gas exsolution.

In general, we can say that, at increasing $CaCO_3$, the role of homogenisation and water content becomes less important and the gas phase is mainly carbon dioxide produced by carbonate dissolution.
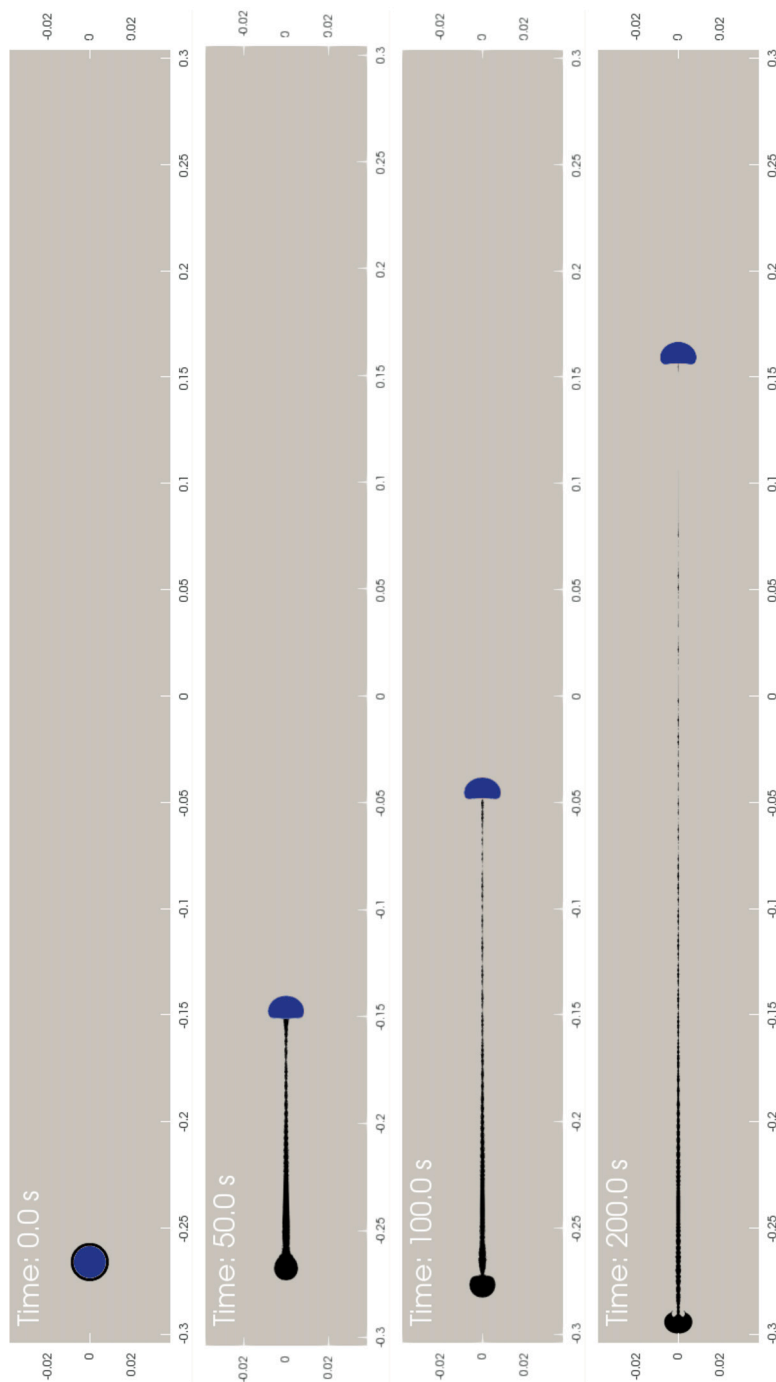
Fig. 5. Mingling simulations at 100 Pa s. See Fig. 4 for an explanation.

5. Discussions

5.1. Carbonate dissolution

The phase diagram of $CaCO_3$ (Baker, 1962; Peretyazhko et al., 2021; Hou et al., 2019) shows that temperature of carbonate decomposition rapidly increases with pressure, hence pure thermal decomposition can take place in the plumbing system only at a very shallow depth. The effect on eruptive style and ascent dynamics is therefore limited. Moreover, a thermal decomposition timescale of a few minutes for small (millimetric-sized) clasts (Knuever et al., 2023) is then extremely large compared with the typical timescales of magma ascent in the upper part of the conduits during explosive eruptions (<1 minute, Colucci

et al. (2017); Colucci and Papale (2021)). Therefore, syn-eruptive dynamics are more probably affected by the carbonate dissolution (i.e., interface reaction + diffusion), as also confirmed by experiments (Deegan et al., 2010; Jolis et al., 2013; Deegan et al., 2022). This finding moves the focus of our investigation from the purely thermal heating of the carbonate clast to the interface reaction and the subsequent diffusion through the melt shell.

Since carbonate dissolution can be considered a diffusion-controlled process, the mobility of CaO is of paramount importance. A constant diffusion coefficient cannot explain the experimental observations, so it became necessary to look for a concentration-dependent expression. The functional form of the diffusion coefficient of CaO, that best fits the dissolution experiments, exponentially decays with decreasing con-
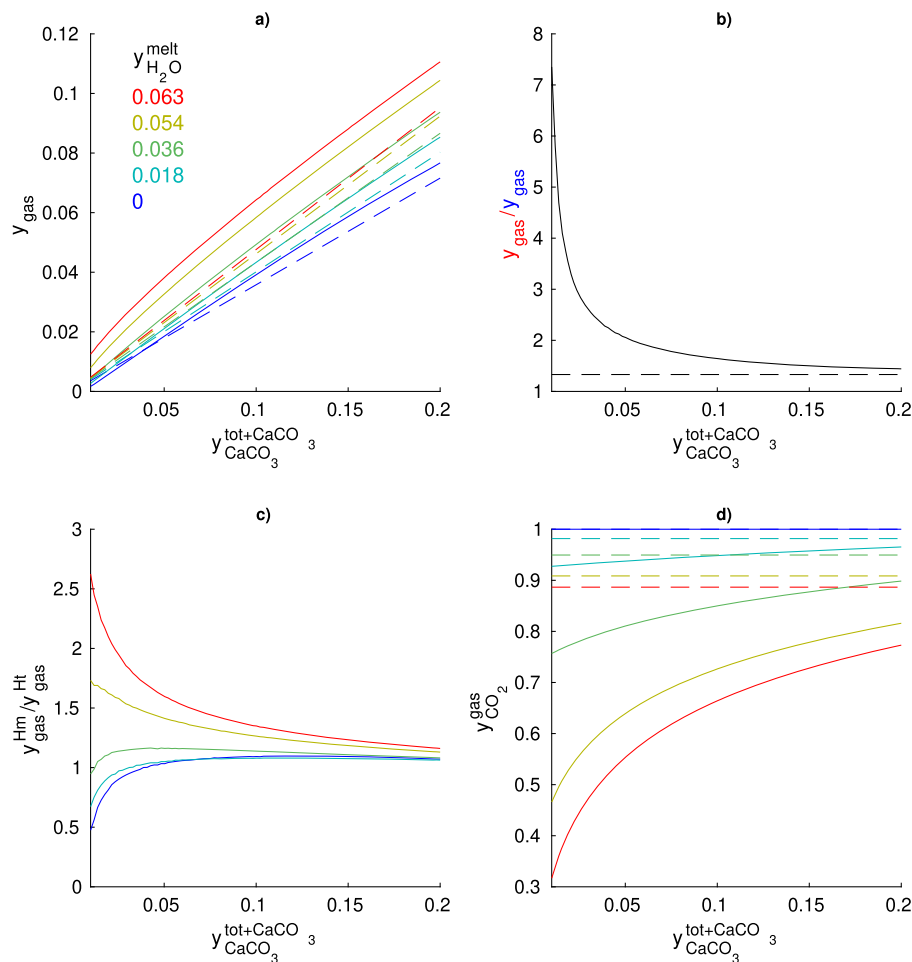
Fig. 6. Thermodynamics of melt-volatile equilibria at 200 MPa and 1273 K. On the horizontal axis, the mass fraction of $CaCO_3$ added to the system; colours from red to blue indicate water content expressed as the mass fraction of dissolved H_2O; dashed lines: heterogeneous system; solid lines: homogeneous system. a) Gas mass fraction; b) ratio between the gas mass generated by carbonate dissolution in a water-saturated host magma and the gas mass generated in an anhydrous host magma (i.e., ratio between red and blue lines of subfigure a); c) ratio between the gas mass generated by carbonate dissolution in the homogeneous and heterogeneous systems (i.e., ratio between solid and dashed lines of subfigure a); d) mass fraction of CO_2 in the gas phase.

centration, from 10^{-7} m^2/s (~35 wt% CaO) to 10^{-11} m^2/s (~10 wt% CaO). Such a functional form of the diffusion coefficient can explain the concentration profile of CaO (i.e., CaO pile-up, Deegan et al. (2010)) and the extremely fast dissolution rate of carbonate measured during magma-carbonate interaction experiments (Deegan et al., 2010; Jolis et al., 2013; Blythe et al., 2015; Hamann et al., 2018). On the other side, we find that a constant diffusion coefficient (D $\approx 10^{-11}$ m^2/s) provides an excellent prediction of the mixing experiments of Deegan et al. (2010). Therefore, it seems that the behaviour of the diffusion coefficient derived from carbonate dissolution experiments differs from the one calculated from mixing experiments. An interesting result about the functional form of the diffusion coefficient of CaO was recently reported in Persikov et al. (2022). These authors calculate from mixing experiments the concentration dependence of all diffusing components at the interaction between a basalt and a carbonate-containing kimberlite melt, using an exponential functional form of the diffusion coefficient very similar to our own. Persikov et al. (2022) conclude that the dependence of the diffusion coefficient of CaO (as well as the other oxides) on concentration is so weak that can be considered constant. Again, this is in contrast with modelling and observations for the dissolution process but in good agreement with experiments and model results for the mixing process.

Some experiments show a network of melt veins intruding the carbonate clast, probably due to a set of original mineral cleavages (Deegan et al., 2010). This could increase the carbonate-melt reaction interface speeding up the dissolution. However, there is no experimental evidence that the original clast is dissected into many smaller dissolving fragments, as expected from a dissolution process acting on both the internal (i.e. fractures) and external surfaces of the original clast. Only a single fragment is visible in the experimental images at the final stages of the dissolution process. Probably, the veins within the clasts are quite thin so they are saturated fast by dissolution, preventing the reaction from continuing. In any case, such a mechanism could explain the fast dissolution rates but it could not justify the shape of the concentration profile (i.e., CaO pile-up).

A possible way to solve this contradiction is to hypothesize that what we estimate during carbonate dissolution experiments is a transient strain-enhanced diffusion (Dickinson et al., 1994; Lim et al., 2000), where the strain is produced by the extensive nucleation and growth of CO_2-rich gas bubbles at the carbonate-melt interface. Interestingly, this effect shall cease when the carbonate is completely dissolved and hence would justify a constant diffusion coefficient for the mixing process. However, further experimental and modelling investigations are required to test this hypothesis.

5.2. Efficiency of gas release during magma-carbonate interaction

Our results show that mingling and mixing between the contaminated melt and the host magma modulate the gas exsolution process in space and time. Bubble trails observed in the experiments at the contamination front are the evidence. These bubbles are explained in the literature as bubbles generated at the carbonate-melt interface and migrated outward (Deegan et al., 2010; Jolis et al., 2013; Blythe et al., 2015). We show, instead, that the concomitant diffusion and exsolution of the volatile species at the contamination front, during mixing, generate a gas wave expanding inward and outward from the front. Also, the CO_2 gas bubbles that migrate outside of the contaminated region interact with the uncontaminated melt, extracting H_2O and yielding CO_2. These two processes, which we shall hereafter call homogenisation-induced exsolution, modulate the availability of exsolved gas in the system and drive the system towards homogenisation. Thermodynamic modelling shows that homogenisation-induced exsolution is more important at small quantities of interacting carbonate. Hence, the timescales of mingling and mixing dictate the timescale of the exsolution process at low values of interacting carbonate. On the other hand, for a larger mass fraction of interacting carbonate, the contribution to the gas phase from the homogenisation (as well as the water content of the host magma) is negligible compared to the primary amount of gas resulting from the carbonate dissolution. In this case, the leading timescale is that of the dissolution.

Let us place these results in a volcanological context. The upper-end limit of 20 wt% of interacting $CaCO_3$, used for thermodynamic calculations, can be representative of a carbonate lithic cargo almost completely dissolving in the host melt in syn-eruptive regime (Sottili et al., 2009) or representative of the carbonate rocks assimilated in plutonic environments (Iacono Marziano et al., 2007). Such an amount of interacting $CaCO_3$ releases a very large amount of gas, even at undersaturated conditions (up to ~30 vol% at 200 MPa and 1473 K, for the Merapi basalt composition). Since the contribution of gas from the homogenisation-induced exsolution is negligible, the timescale of gas release will depend essentially on the dissolution rate of the carbonate clasts. The timescale of this process is on the order of seconds to minutes for clasts <1 cm and becomes much longer (days) for larger sizes. In a syn-eruptive scenario, the conditions leading to an extensive dissolution of the carbonate lithics may be related to a finer size distribution of carbonate lithics. In this case, the release of a large amount of gas in such a short time may trigger an eruptive event or drive mafic magmas towards anomalously high-intensity explosive eruptions (La Spina et al., 2022).

Most times, we expect only a percentage of the carbonate to be assimilating. For example, in the Colli Albani district (Italy), entrained carbonate lithics show variable degrees of interaction (Sottili et al., 2010) and their size distribution lacks the finer classes (Sottili et al., 2009). Also, the assimilation itself, as will be discussed later, can be a self-limiting process. Thus, the value of ~5 wt%, used in our thermodynamic calculations, can be considered representative of these situations. At such conditions, mixing and mingling processes play a central role in determining the efficiency of volatile exsolution eventually enhancing the explosivity of an eruptive event. Simulation results suggest that the effect of increasing viscosity of the host melt is to slow down homogenisation, hence having a buffering effect on the homogenisation-induced volatile exsolution. On the other hand, at low viscosities most gas can be exsolved right at the beginning of the magmatic interaction, possibly contributing to an increase in the explosivity of mafic, crystal-free magmatic systems. Even considering the higher viscosity case, thermodynamic modelling shows that dissolution of carbonate can release, at 200 MPa and 1473 K (Merapi basalt composition) ~10 vol. % of gas. Such an amount may still impact the eruption style determining the transition from effusive to explosive (La Spina et al., 2022) or unresting episodes.

Anyway, it is worth noting that in our models we assumed isothermal superliquidus conditions. While this assumption works for model comparison with the experiments, temperature variations due, for example, to the ingestion of a high amount of cold carbonate, could be important, in particular during the emplacement in the crust. As temperature decreases, diffusion slows down and viscosity increases, hindering dissolution, mingling and mixing dynamics. In this situation, carbonate dissolution and mingling could have similar timescales ($\tau_{dis} \simeq \tau_{min}$) and bubbles can migrate while the carbonate is still dissolving. Multiple smaller bubbles rising, instead of a single or few larger bubbles, could change mingling dynamics, favouring chaotic mixing (Wiesmaier et al., 2015). Temperature decrease below liquidus can induce crystallisation. Crystallisation of the magma also increases with increasing carbonate assimilation (Iacono Marziano et al., 2007; Carter and Dasgupta, 2016). While the dissolution timescale seems to be unaffected by limestone composition (i.e., CaO vs MgO) (Jolis et al., 2013), the MgO content can control the crystallisation process and the evolution of the residual melt (Iacono Marziano et al., 2007). Crystallisation increases the melt + crystals mixture viscosity, hindering mingling and mixing. In summary, temperature can play an important role in the magma-carbonate interaction and the assimilation of carbonate becoming a self-limiting process over a relatively long time (i.e., hours to days in Iacono Marziano et al. (2007)). Fingerprints of short-term magma-carbonate interaction preserved in the deposits confirm a possible incomplete homogenisation process between magma and carbonate. For example, Morris and Canil (2021) observe drops of contaminated, Ca-rich melts in the mafic dikes of the Jurassic Bonanza arc, hypothesizing that it can be the result of an incomplete homogenisation process between magma and carbonate; also, the primary, magmatic calcite in the groundmass of lava flows in the Colli Albani volcanic district (Italy) (Gozzi et al., 2014) may have crystallized from drops of contaminated melt, remnants of slow mingling and mixing processes.

6. Conclusions

- Short-term interaction of magma with carbonate has important effects on volatile exsolution. Lithic clasts dissolve in the magma generating contaminated Ca-, CO_2-rich melt pockets with a primary CO_2-dominated gas phase. The mingling and mixing processes between these contaminated melt pockets and the host melt lead the system to homogenisation and modulate the amount of exsolved gas.
- At larger amounts of interacting carbonate, the contribution of gas from homogenisation is negligible compared to the primary gas exsolution resulting from carbonate dissolution. Hence, the leading timescale is that of dissolution. In this case, a large amount of gas can be produced (up to $\sim$ 30 vol% at 200 MPa and 1473 K, from dissolution of $\sim$ 20 wt% of carbonate) in a short time (seconds to minutes for millimetric clasts), driving mafic magmas towards anomalously high-intensity explosive eruptions or determining volcanic unrest.
- At low quantities of interacting carbonate, the homogenisation process contributes more to the gas amount of the system, hence, the timescales of mingling and mixing dictate the timescale of exsolution. Likely the system never reaches homogenisation in syn-eruptive regimes, due to the relatively slower homogenisation process. Even in this case, dissolution of carbonate can release, at 200 MPa and 1473 K, $\sim$ 10 vol% of gas. Such an amount may still impact the eruption style determining the transition from effusive to explosive or volcanic unrest.
- Slower mixing and mingling due to greater host magma viscosities imply that the fingerprints of short-term magma-carbonate interaction can be preserved in the volcanic deposits, in the form of filaments or drops of contaminated melt.

- Future model developments include simulating the scenario where carbonate dissolution and bubble-enhanced mingling happen on similar timescales. However, further work is required to understand the kinetics of dissolution of carbonate. We think that the anomalous high mobility of CaO, obtained from carbonate dissolution experiments, in contrast with the one measured during the diffusion couple experiments, merits attention.

CRediT authorship contribution statement

Simone Colucci: Writing – review & editing, Writing – original draft, Visualization, Validation, Supervision, Software, Methodology, Investigation, Formal analysis, Data curation, Conceptualization. **Federico Brogi:** Writing – review & editing, Writing – original draft, Visualization, Validation, Software, Methodology, Investigation, Formal analysis, Data curation. **Gianluca Sottili:** Writing – review & editing. **Chiara P. Montagna:** Writing – review & editing. **Paolo Papale:** Writing – review & editing.

Declaration of competing interest

The authors declare that they have no known competing financial interests or personal relationships that could have appeared to influence the work reported in this paper.

Code and data availability

The matlab scripts used for modelling dissolution and mixing are archived on Zenodo (MagmaMixingModel: https://doi.org/10.5281/zenodo.10523077; Dissolution-growth model: https://doi.org/10.5281/zenodo.10522967). SOLWCAD is available at https://www.pi.ingv.it/progetti/eurovolc/. CFD mingling simulations are realized with the open source software OpenFOAM (https://www.openfoam.com/).

Acknowledgements

Appendix A

A.1. Assuming conservation of mass of CaO within a constant-density melt shell (see Table 1 for notations and units)

$$m_{CaO}^{CaCO_3}(t) = m_{CaO}^{CaCO_3}(0) + \rho_{melt}\left[\int_{V_{melt}} y_{CaO}^{melt}(\tilde{x},0)d\tilde{x} - \int_{V_{melt}} y_{CaO}^{melt}(\tilde{x},t)d\tilde{x}\right]. \tag{A.1}$$

The substitution $\tilde{x} = 4/3\pi x^3$, where x is the Lagrangian coordinate (eq. (3)), yields $d\tilde{x} = 4\pi x^2 dx$. Therefore,

$$m_{CaO}^{CaCO_3}(t) = m_{CaO}^{CaCO_3}(0)$$
$$+ 4\pi\rho_{melt}\left[\int_{R_0}^{S_0} y_{CaO}^{melt}(x,0)x^2 dx - \int_{R_0}^{S_0} y_{CaO}^{melt}(x,t)x^2 dx\right]. \tag{A.2}$$

Derivating in time,

$$\frac{dm_{CaO}^{CaCO_3}}{dt} = 4\pi\rho_{melt}\int_{R_0}^{S_0}\left[\frac{dy_{CaO}^{melt}}{dt}x^2\right]dx. \tag{A.3}$$

Considering that

$$\frac{m_{CaO}^{CaCO_3}}{\varepsilon_{CaO}} = m_{CaCO_3} = \frac{4}{3}\pi R^3 \rho_{CaCO_3}, \tag{A.4}$$

we obtain

$$\frac{dR^3}{dt} = \frac{3}{\varepsilon_{CaO}}\frac{\rho_{melt}}{\rho_{CaCO_3}}\int_{R_0}^{S_0}x^2\frac{dy_{CaO}^{melt}}{dt}dx. \tag{A.5}$$

Appendix B

B.1. Equation (7) for an infinite diffusion couple can be solved analytically (Kulkarni, 2021). The infinite diffusion couple is defined by the following initial and boundary conditions

$$\mathbf{y}(x < 0, 0) = \mathbf{y}^-, \tag{B.1}$$

$$\mathbf{y}(x > 0, 0) = \mathbf{y}^+, \tag{B.2}$$

$$\mathbf{y}(-\infty, t) = \mathbf{y}^-, \tag{B.3}$$

$$\mathbf{y}(+\infty, t) = \mathbf{y}^+, \tag{B.4}$$

where $\mathbf{y}^-$ and $\mathbf{y}^+$ are, respectively, the vectors of the composition at the left and the right terminal of the diffusion couple. The solution of equation (7) reads

$$\mathbf{y} = \bar{\mathbf{y}} + \frac{1}{2}\mathbf{PFP}^{-1}\Delta\mathbf{y} \tag{B.5}$$

Here, $\bar{\mathbf{y}}$ is the vector of the mean terminal concentrations ($\bar{y}_i = (y_i^+ + y_i^-)/2$), $\Delta\mathbf{y}$ is the vector of the difference between terminal concentrations ($\Delta y_i = y_i^+ - y_i^-$), $\mathbf{P}$ is the matrix whose columns are the eigenvectors of $\mathbf{D}$ and $\mathbf{F}$ is a diagonal matrix

$$F = \begin{pmatrix} erf\left(\frac{x}{2\sqrt{\lambda_1 t}}\right) & \cdots & \cdots & 0 \\ \vdots & \ddots & & \vdots \\ \vdots & & \ddots & \vdots \\ 0 & \cdots & \cdots & erf\left(\frac{x}{2\sqrt{\lambda_{n-1}t}}\right) \end{pmatrix}$$

where λ_i are the eigenvalues of $\mathbf{D}$.

B.2. The exsolution/dissolution term can be written as the product between the interfacial mass flux J and the interfacial area concentration A

$$\Gamma_i = J_i A, \quad i = H_2O, CO_2. \tag{B.6}$$

Considering a representative spherical bubble of radius R [m], and a bubble number density N_b (number of bubbles per unit volume of liquid), the interfacial area concentration A [m^2/m^3] is given by

$$A = 4\pi R^2 N_b(1 - \alpha). \tag{B.7}$$

The interfacial mass flux [kg/(m^2 s)] is given by

$$J_i = \rho_{melt}\alpha D_i\left[\frac{dy_i^{melt}}{dr}\right]_R, \tag{B.8}$$

where the term in square brackets is the derivative at the bubble-melt interface. For an isolated bubble, under quasi-static approximation, it is given by (see Appendix B.3)

$$\left[\frac{dy_i^{melt}}{dr}\right]_R = \frac{\left(y_i^{melt} - \tilde{y}_i^{melt}\left(y_{SiO_2}^{melt}, ..., y_{H_2O}^{tot}, y_{CO_2}^{tot}\right)\right)}{R},$$ (B.9)

where $\tilde{y}_i^{melt}$ is given by the SOLWCAD model (Papale et al., 2006) as a function of the melt composition and total volatile content.

B.3. The transfer of the i-th volatile species in the melt shell around a growing bubble is described by the advection-diffusion equation in a spherical coordinate system centred at the centre of the bubble

$$\frac{\partial y_i^{melt}}{\partial t} + u_r \frac{\partial y_i^{melt}}{\partial r} = \frac{1}{r^2}\frac{\partial}{\partial r}\left(r^2 D_i \frac{\partial y_i^{melt}}{\partial r}\right),$$ (B.10)

where y_i^{melt} is the concentration of species i in the melt, D_i is the species diffusion coefficient, and u_r is the radial velocity in the melt due to bubble growth. When advection time is larger than diffusion time (Peclet number << 1), the left-hand side of Eq. (B.10) vanishes, and concentration distribution is quasi-static

$$\frac{1}{r^2}\frac{d}{dr}\left(Dr^2\frac{dy_i^{melt}}{dr}\right) = 0.$$ (B.11)

By applying the product rule and assuming constant D we obtain

$$\frac{D}{r^2}\left[2r\frac{dy_i^{melt}}{dr} + r^2\frac{dy_i^{melt}}{dr^2}\right] = 0.$$ (B.12)

Applying the substitution $z = dy_i^{melt}/dr$ we obtain a first-order ODE

$$\frac{dz}{dr} = -\frac{2}{r}z$$ (B.13)

that can be solved by the separation of variables, obtaining

$$z = \frac{dy_i^{melt}}{dr} = \frac{C}{r^2}.$$ (B.14)

The general solution is

$$y_i^{melt}(r) = A - \frac{B}{r}.$$ (B.15)

For an isolated bubble, under local thermodynamic equilibrium assumption (i.e., at the bubble-melt interface gas and liquid are at thermodynamic equilibrium), the boundary conditions at the bubble-melt interface (r = R) and the shell wall (r = S) are given by

$$y_i^{melt}(r = R) = \tilde{y}_i^{melt}$$ (B.16)

$$y_i^{melt}(r = S) = y_s,$$ (B.17)

obtaining

$$A = \tilde{y}_i^{melt} + \frac{B}{R}$$ (B.18)

$$B = \left(y_s - \tilde{y}_i^{melt}\right)R.$$ (B.19)

The value of the derivative at the interface with the bubble in equation (B.8) can now be calculated

$$\left[\frac{dy_i^{melt}}{dr}\right]_R = \frac{\left(y_s - \tilde{y}_i^{melt}\right)}{R},$$ (B.20)

B.4. The effective binary diffusion coefficient of H_2O is given by Freda et al. (2003)

Table C.3
Liquid properties for the experiment of Kemiha et al. (2007) used here for validation of the OpenFOAM multiphase solver selected for this study. The interfacial tension between the two liquids is 14.2×10^{-3} (N/m).

fluid	viscosity (Pa s)	density (kg/m^3)	surface tension x10^{-3} (N/m)
silicon oil	0.1	965	20.2
Emkarox 65% (wt)	0.625	1052	38.7

$$D_{H_2O} = \exp\left[-11.924 - 1.003 \cdot \ln\left(100 \cdot y_{H_2O}^{melt}\right)\right]$$
$$\times \exp\left[\frac{-\exp\left(11.836 - 0.139 \cdot \ln(100 \cdot y_{H_2O}^{melt})\right)}{\tilde{R}T}\right]$$ (B.21)

where T is in kelvins, $y_{H_2O}^{melt}$ is the weight fraction of dissolved water and $\tilde{R}$ is the universal gas constant. Equation (B.21) may be applied to trachyte, as well as basalt (Georgeais et al., 2021), at 1373 – 1673 K, p = 1 GPa and y_{H_2O} between 0.0025 and 0.02.

The effective binary diffusion coefficient of CO_2 is given by Zhang et al. (2007)

$$D_{CO_2} = \exp\left[-13.99 - \frac{(17367 + 1.9448 \cdot p)}{T} + 100 \cdot y_{H_2O}^{melt}\frac{(855.2 + 0.2712 \cdot p)}{T}\right],$$ (B.22)

where p is in MPa and T is in kelvins. Equation (B.22) may be applied from rhyolite to basalt, at 773–1773 K, p ≤ 1 GPa and $y_{H_2O}^{melt} \leq 0.05$ wt%.

Appendix C

C.1. The multiphase fluid dynamic OpenFOAM solver icoReactingMultiphaseInterFoam is used in this work to study the mingling driven by a rising gas bubble. In order to assess its capability in reproducing bubble-induced mingling we consider the experiments of Kemiha et al. (2007) (Fig. C.7). In this work, experiments and numerical simulations are used to study the evolution of a liquid-liquid interface following the passage of a rising bubble, matching quite well the subject of the present investigation. In the experimental setup, a gas bubble (d = 5.1 mm) is released from a submerged orifice at the bottom of a glass tank (12 cm width, 50 cm high) filled with two Newtonian liquids of different densities, viscosities, and surface tensions (Table C.3). In particular, a lighter and less viscous liquid (silicon oil) is placed on top of a heavier and more viscous one (a dilute solution of the lubricant Emkarox HV45 and demineralized water). In addition, an interfacial tension is also present between the two liquids, the effect of which has not been considered in the simulations with silicate melts.

Before impacting the liquid-liquid interface the rising bubble has covered enough distance to reach its terminal velocity (in the lower liquid). As a result, the size of the computational domain was chosen accordingly. In order to reduce the computational effort, also here we used an axisymmetric setup with a Free-slip boundary condition for the lateral boundary and no slip for the top and bottom boundaries. Overall, the numerical solution and the experiment are in very good agreement, given the uncertainties in the experimental conditions (Fig. C.7). Both the position of the bubble and the geometry of the liquid-liquid interface for similar times are well reproduced by the numerical solver, even if the time "zero" in the simulation was roughly chosen by looking at the position of the bubble in the first experimental image. Therefore, although some differences can be clearly noticed, especially at later times, the qualitative comparison is more than satisfactory.
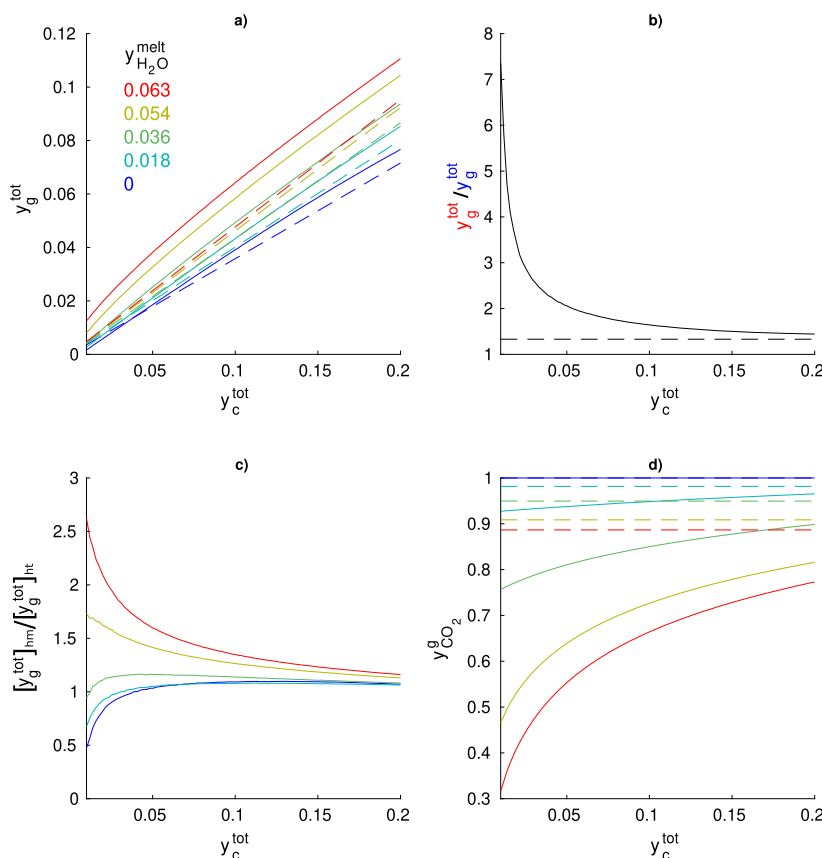
Fig. C.7. Comparison between snapshots at different times from a numerical simulation, and the image sequences of an experiment for a rising bubble that crosses the interface separating two liquids with different densities, viscosities and surface tensions (Kemiha et al., 2007). Unlike previous simulations, an interfacial tension between the two liquids is also present.

References

Baker, D.R., Freda, C., Brooker, R., Scarlato, P., 2005. Volatile diffusion in silicate melts and its effects on melt inclusions. Ann. Geophys. 48. https://doi.org/10.4401/ag-3227.

Baker, E., 1962. 87. The calcium oxide–carbon dioxide system in the pressure range 1—300 atmospheres. J. Chem. Soc. (Resumed), 464–470.

Blythe, L.S., Deegan, F.M., Freda, C., Jolis, E.M., Masotta, M., Misiti, V., Taddeucci, J., Troll, V.R., 2015. CO_2 bubble generation and migration during magma-carbonate interaction. Contrib. Mineral. Petrol. 169, 42. https://doi.org/10.1007/s00410-015-1137-4.

Brogi, F., Colucci, S., Matrone, J., Montagna, C.P., De' Michieli Vitturi, M., Papale, P., 2022. Magmafoam-1.0: a modular framework for the simulation of magmatic systems. Geosci. Model Dev. 15, 3773–3796. https://doi.org/10.5194/gmd-15-3773-2022.

Caricchi, L., Burlini, L., Ulmer, P., Gerya, T., Vassalli, M., Papale, P., 2007. Non-Newtonian rheology of crystal-bearing magmas and implications for magma ascent dynamics. Earth Planet. Sci. Lett. 264, 402–419. https://doi.org/10.1016/j.epsl.2007.09.032.

Carter, L.B., Dasgupta, R., 2016. Effect of melt composition on crustal carbonate assimilation: implications for the transition from calcite consumption to skarnification and associated co2 degassing. Geochem. Geophys. Geosyst. 17, 3893–3916. https://doi.org/10.1002/2016GC006444.

Cella, F., Fedi, M., Florio, G., Grimaldi, M., Rapolla, A., 2007. Shallow structure of the Somma–Vesuvius Volcano from 3d inversion of gravity data. J. Volcanol. Geotherm. Res. 161, 303–317. https://doi.org/10.1016/j.jvolgeores.2006.12.013.

Colucci, S., Papale, P., 2021. Deep magma transport control on the size and evolution of explosive volcanic eruptions. Front. Earth Sci. 9. https://doi.org/10.3389/feart.2021.681083.

Colucci, S., Papale, P., Montagna, C.P., 2017. Non-Newtonian flow of bubbly magma in volcanic conduits. J. Geophys. Res., Solid Earth 122, 1789–1804. https://doi.org/10.1002/2016JB013383.

Cussler, E.L., 2007. Diffusion Mass Transfer in Fluid Systems, 3rd ed. Cambridge University Press.

Deegan, F.M., Bédard, J.H., Grasby, S.E., Dewing, K., Geiger, H., Misiti, V., Capriolo, M., Callegaro, S., Svensen, H.H., Yakymchuk, C., Aradi, L.E., Freda, C., Troll, V.R., 2022. Magma–shale interaction in large igneous provinces: implications for climate warming and sulfide genesis. J. Petrol. 63, egac094. https://doi.org/10.1093/petrology/egac094. arXiv:https://academic.oup.com/petrology/article-pdf/63/9/egac094/51333588/egac094.pdf.

Deegan, F.M., Troll, V.R., Freda, C., Misiti, V., Chadwick, J.P., McLeod, C.L., Davidson, J.P., 2010. Magma–carbonate interaction processes and associated CO2 release at Merapi Volcano, Indonesia: insights from experimental petrology. J. Petrol. 51, 1027–1051. https://doi.org/10.1093/petrology/egq010.

Deegan, F.M., Troll, V.R., Gertisser, R., Freda, C., 2023. Magma-Carbonate Interaction at Merapi Volcano, Indonesia. Springer International Publishing, Cham, pp. 291–321.

Di Rocco, T., Freda, C., Gaeta, M., Mollo, S., Dallai, L., 2012. Magma chambers emplaced in carbonate substrate: petrogenesis of skarn and cumulate rocks and implications for CO2 degassing in volcanic areas. J. Petrol. 53, 2307–2332. https://doi.org/10.1093/petrology/egs051.

Dickinson, J.T., Jensen, L.C., Langford, S.C., Dion, R.P., 1994. Emission of occluded volatiles during deformation of polycarbonate due to strain-enhanced diffusion. J. Polym. Sci., Part B, Polym. Phys. 32, 993–999. https://doi.org/10.1002/polb.1994.090320604.

Freda, C., Baker, D.R., Romano, C., Scarlato, P., 2003. Water Diffusion in Natural Potassic Melts. Special Publications, vol. 213. Geological Society, London, pp. 53–62.

Freda, C., Gaeta, M., Giaccio, B., Marra, F., Palladino, D.M., Scarlato, P., Sottili, G., 2011. Co_2-driven large mafic explosive eruptions: the pozzolane rosse case study from the colli albani volcanic district (Italy). Bull. Volcanol. 73, 241–256. https://doi.org/10.1007/s00445-010-0406-3.

Gaeta, M., Di Rocco, T., Freda, C., 2009. Carbonate assimilation in open magmatic systems: the role of melt-bearing skarns and cumulate-forming processes. J. Petrol. 50, 361–385. https://doi.org/10.1093/petrology/egp002.

Georgeais, G., Koga, K.T., Moussallam, Y., Rose-Koga, E.F., 2021. Magma decompression rate calculations with ember: a user-friendly software to model diffusion of h2o, co2, and s in melt embayments. Geochem. Geophys. Geosyst. 22, e2020GC009542. https://doi.org/10.1029/2020GC009542.

Giordano, D., Russell, J., Dingwell, D., 2008. Viscosity of magmatic liquids: a model. Earth Planet. Sci. Lett. 271, 123–134.

Goff, F.E., Love, S.P., Warren, R.G., Counce, D.A., Obenholzner, J.H., Siebe, C., Schmidt, S.C., 2001. Passive infrared remote sensing evidence for large, intermittent co2 emissions at Popocatépetl Volcano, Mexico. Chem. Geol. 177, 133–156.

González-García, D., Behrens, H., Petrelli, M., Vetere, F., Morgavi, D., Zhang, C., Perugini, D., 2017. Water-enhanced interdiffusion of major elements between natural shoshon-

ite and high-k rhyolite melts. Chem. Geol. 466, 86–101. https://doi.org/10.1016/j.chemgeo.2017.05.023.

Gozzi, F., Gaeta, M., Freda, C., Mollo, S., Di Rocco, T., Marra, F., Dallai, L., Pack, A., 2014. Primary magmatic calcite reveals origin from crustal carbonate. Lithos 190–191, 191–203. https://doi.org/10.1016/j.lithos.2013.12.008.

Guo, C., Zhang, Y., 2020. Multicomponent diffusion in a basaltic melt: temperature dependence. Chem. Geol. 549, 119700. https://doi.org/10.1016/j.chemgeo.2020.119700.

Hamann, C., Bläsing, S., Hecht, L., Schäffer, S., Deutsch, A., Osterholz, J., Lexow, B., 2018. The reaction of carbonates in contact with laser-generated, superheated silicate melts: constraining impact metamorphism of carbonate-bearing target rocks. Meteorit. Planet. Sci. 53, 1644–1686. https://doi.org/10.1111/maps.13133.

Hofmann, A.W., Magaritz, M., 1977. Diffusion of ca, sr, ba, and co in a basalt melt: implications for the geochemistry of the mantle. J. Geophys. Res. 82, 5432–5440. https://doi.org/10.1029/JB082i033p05432. https://agupubs.onlinelibrary.wiley.com/doi/abs/10.1029/JB082i033p05432. arXiv:https://agupubs.onlinelibrary.wiley.com/doi/pdf/10.1029/JB082i033p05432.

Hou, M., Zhang, Q., Tao, R., Liu, H., Kono, Y., Mao, H.k., Yang, W, Chen, B., Fei, Y., 2019. Temperature-induced amorphization in caco3 at high pressure and implications for recycled caco3 in subduction zones. Nat. Commun. 10, 1963. https://doi.org/10.1038/s41467-019-09742-5.

Iacono-Marziano, G., Gaillard, F., Scaillet, B., Pichavant, M., Chiodini, G., 2009. Role of non-mantle CO2 in the dynamics of volcano degassing: the Mount Vesuvius example. Geology 37, 319–322. https://doi.org/10.1130/G25446A.1.

Iacono Marziano, G., Schmidt, B.C., Dolfi, D., 2007. Equilibrium and disequilibrium degassing of a phonolitic melt (Vesuvius ad 79 "white pumice") simulated by decompression experiments. J. Volcanol. Geotherm. Res. 161, 151–164. https://doi.org/10.1016/j.jvolgeores.2006.12.001.

Jolis, E., Freda, C., Troll, V., Deegan, F., Blythe, L., McLeod, C., Davidson, J., 2013. Experimental simulation of magma-carbonate interaction beneath Mt. Vesuvius, Italy. Contrib. Mineral. Petrol. 166, 1335–1353. https://doi.org/10.1007/s00410-013-0931-0.

Kemiha, M., Olmos, E., Fei, W., Poncin, S., Li, H.Z., 2007. Passage of a gas bubble through a liquid- liquid interface. Ind. Eng. Chem. Res. 46, 6099–6104.

Knuever, M., Sulpizio, R., Mele, D., Pisello, A., Costa, A., Perugini, D., Vetere, F., 2023. Decarbonation and clast dissolution timescales for short-term magma-carbonate interactions in the volcanic feeding system and their influence on eruptive dynamics: insights from experiments at atmospheric pressure. Chem. Geol. 639, 121724. https://doi.org/10.1016/j.chemgeo.2023.121724.

Knuever, M., Sulpizio, R., Mele, D., Costa, A., 2022. Magma–Rock Interactions: a Review of Their Influence on Magma Rising Processes with Emphasis on Short-Timescale Assimilation of Carbonate Rocks. Special Publications, vol. 520. Geological Society, London.

Kulkarni, K.N., 2021. Analytical solution for interdiffusion in multicomponent systems and its application in high entropy alloys. AIP Adv. 11 (1), 015116. https://doi.org/10.1063/5.0032837.

La Spina, G., Arzilli, F., Burton, M., Polacci, M., Clarke, A., 2022. Role of volatiles in highly explosive basaltic eruptions. Commun. Earth Environ. 3, 156. https://doi.org/10.1038/s43247-022-00479-6.

Lim, Y.S., Lee, J.Y., Kim, H.S., Moon, D.W., 2000. Strain-induced diffusion in a strained $Si1 - xGex/Si$ heterostructure. Appl. Phys. Lett. 77, 4157–4159. https://doi.org/10.1063/1.1327280.

Lustrino, M., Luciani, N., Stagno, V., Narzisi, S., Masotta, M., Scarlato, P., 2022. Experimental evidence on the origin of Ca-rich carbonated melts formed by interaction between sedimentary limestones and mantle-derived ultrabasic magmas. Geology 50, 476–480. https://doi.org/10.1130/G49621.1.

Mollo, S., Gaeta, M., Freda, C., Di Rocco, T., Misiti, V., Scarlato, P., 2010. Carbonate assimilation in magmas: a reappraisal based on experimental petrology. Lithos 114, 503–514. https://doi.org/10.1016/j.lithos.2009.10.013.

Morris, R., Canil, D., 2021. Co2 transport at shallow depths in arc magmas: evidence from unique orbicular dikes in the Jurassic bonanza arc, Vancouver Island, Canada. Contrib. Mineral. Petrol. 177. https://doi.org/10.1007/s00410-021-01852-y.

Nowak, M., Schreen, D., Spickenbom, K., 2004. Argon and co2 on the race track in silicate melts: a tool for the development of a co2 speciation and diffusion model. Geochim. Cosmochim. Acta 68, 5127–5138. https://doi.org/10.1016/j.gca.2004.06.002. structure and Properties of Siliate Melts and Fluids.

Onsager, L., 1945. Theories and problems of liquid diffusion. Ann. N.Y. Acad. Sci. 46 (5), 241. https://doi.org/10.1111/j.1749-6632.1945.tb36170.x.

Papale, P., Moretti, R., Barbato, D., 2006. The compositional dependence of the saturation surface of $H_2O + CO_2$ fluids in silicate melts. Chem. Geol. 229, 78–95.

Papale, P., Moretti, R., Paonita, A., 2022. Thermodynamics of multi-component gas–melt equilibrium in magmas: theory, models, and applications. Rev. Mineral. Geochem. 87, 431–556. https://doi.org/10.2138/rmg.2022.87.10.

Peretyazhko, I.S., Savina, E.A., Khromova, E.A., 2021. Low-pressure (>4 mpa) and high-temperature (>1250 °C) incongruent melting of marly limestone: formation of carbonate melt and melilite–nepheline paralava in the khamaryn–khural–khiid combustion metamorphic complex, East Mongolia. Contrib. Mineral. Petrol. 176. https://doi.org/10.1007/s00410-021-01794-5.

Persikov, E., Bukhtiyarov, P., Nekrasov, A., 2022. Experimental study of the multi-component chemical diffusion of major components (sio2, al2o3, na2o, cao, mgo, and feo) and the $co2 - 3$ anion at interaction between basalt and kimberlite melts under a moderate pressure. Petrology 30, 325–335. https://doi.org/10.1134/S0869591122020060.

Sottili, G., Taddeucci, J., Palladino, D., 2010. Constraints on magma–wall rock thermal interaction during explosive eruptions from textural analysis of cored bombs. J. Volcanol. Geotherm. Res. 192, 27–34. https://doi.org/10.1016/j.jvolgeores.2010.02.003.

Sottili, G., Taddeucci, J., Palladino, D., Gaeta, M., Scarlato, P., Ventura, G., 2009. Subsurface dynamics and eruptive styles of maars in the colli albani volcanic district, central Italy. J. Volcanol. Geotherm. Res. 180, 189–202. https://doi.org/10.1016/j.jvolgeores.2008.07.022. models and products of mafic explosive activity.

Spickenbom, K., Sierralta, M., Nowak, M., 2010. Carbon dioxide and argon diffusion in silicate melts: insights into the co2 speciation in magmas. Geochim. Cosmochim. Acta 74, 6541–6564. https://doi.org/10.1016/j.gca.2010.08.022.

Troll, V.R., Hilton, D.R., Jolis, E.M., Chadwick, J.P., Blythe, L.S., Deegan, F.M., Schwarzkopf, L.M., Zimmer, M., 2012. Crustal co2 liberation during the 2006 eruption and earthquake events at Merapi Volcano, Indonesia. Geophys. Res. Lett. 39, 10.1029/2012GL051307.

Watson, E.B., Sneeringer, M.A., Ross, A., 1982. Diffusion of dissolved carbonate in magmas: experimental results and applications. Earth Planet. Sci. Lett. 61, 346–358. https://doi.org/10.1016/0012-821X(82)90065-6.

Whitley, S., Halama, R., Gertisser, R., Preece, K., Deegan, F., Troll, V.R., 2020. Magmatic and metasomatic effects of magma-carbonate interaction recorded in calc-silicate xenoliths from Merapi Volcano (Indonesia). J. Petrol. 61. https://doi.org/10.1093/petrology/egaa048.

Wiesmaier, S., Morgavi, D., Renggli, C.J., Perugini, D., De Campos, C.P., Hess, K.U., Ertel-Ingrisch, W., Lavallée, Y., Dingwell, D.B., 2015. Magma mixing enhanced by bubble segregation. Solid Earth 6, 1007–1023. https://doi.org/10.5194/se-6-1007-2015.

Zhang, Y., Gan, T., 2022. Diffusion in melts and magmas. Rev. Mineral. Geochem. 87, 283–337. https://doi.org/10.2138/rmg.2022.87.07. arXiv:https://pubs.geoscienceworld.org/msa/rimg/article-pdf/87/1/283/5595002/rmg.2022.87.07.pdf.

Zhang, Y., Ni, H., 2010. Diffusion of H, C, and O components in silicate melts. Rev. Mineral. Geochem. 72, 171–225. https://doi.org/10.2138/rmg.2010.72.5.

Zhang, Y., Xu, Z., Zhu, M., Wang, H., 2007. Silicate melt properties and volcanic eruptions. Rev. Geophys. 45. https://doi.org/10.1029/2006RG000216.